Top Catal (2016) 59:1305–1318
DOI 10.1007/s11244-016-0654-3

ORIGINAL PAPER

Photocatalytic Activity of Mesoporous Graphitic Carbon Nitride (mpg-C_3N_4) Towards Organic Chromophores Under UV and VIS Light Illumination

Deniz Altunoz Erdogan[1] · Melike Sevim[2] · Ezgi Kısa[3] · Dilara Borte Emiroglu[1] · Mustafa Karatok[1] · Evgeny I. Vovk[1,4] · Morten Bjerring[5] · Ümit Akbey[5,6] · Önder Metin[2] · Emrah Ozensoy[1]

Published online: 11 August 2016

Abstract A template-assisted synthetic method including the thermal polycondensation of guanidine hydrochloride (GndCl) was utilized to synthesize highly-organized mesoporous graphitic carbon nitride (mpg-C_3N_4) photocatalysts. Comprehensive structural analysis of the mpg-C_3N_4 materials were performed by XPS, XRD, FT-IR, BET and solid-state NMR spectroscopy. Photocatalytic performance of the mpg-C_3N_4 materials was studied for the photodegradation of several dyes under visible and UV light illumination as a function of catalyst loading and the structure of mpg-C_3N_4 depending on the polycondensation temperature. Among all of the formerly reported performances in the literature (including the ones for Degussa P25 commercial benchmark), currently synthesized mpg-C_3N_4 photocatalysts exhibit a significantly superior visible light-induced photocatalytic activity towards rhodamine B (RhB) dye. Enhanced catalytic efficiency could be mainly attributed to the terminated polycondensation process, high specific surface area, and mesoporous structure with a wide pore size distribution.

Keywords Graphitic-C_3N_4 · Carbon nitride · UV–Vis light · Photocatalytic degradation · Organic dyes

1 Introduction

Functional materials synthesized by utilizing novel preparation strategies can be promising photocatalytic platforms that harvest renewable solar energy in order to eliminate hazardous industrial contaminants through energy-efficient pathways. Such economic and technological opportunities led to a rapid growth in the research focusing on photocatalytic materials in the recent decades [1–5]. Among such photocatalytic architectures, graphitic carbon nitride (g-C_3N_4) that is the most stable allotrope of carbon nitride at ambient atmosphere stands out as one of the strong contenders in the photocatalytic air and water purification processes owing to its advantageous properties such as being cost-efficient, abundant, non-toxic, metal-free, and stable nature under ambient conditions with a low electronic band gap falling in the visible (VIS) range of the solar spectrum. [5–8]. g-C_3N_4 is a polymeric material which merely consists of two of the most readily accessible elements in the chemical industry, namely C and N, as well as some impurity H revealing a 2D/layered structure with a typical band gap of 2.7 eV which can be excited with VIS

Electronic supplementary material The online version of this article (doi:10.1007/s11244-016-0654-3) contains supplementary material, which is available to authorized users.

✉ Önder Metin
ometin@atauni.edu.tr

✉ Emrah Ozensoy
ozensoy@fen.bilkent.edu.tr

[1] Department of Chemistry, Bilkent University, 06800 Ankara, Turkey

[2] Department of Chemistry, Faculty of Science, Atatürk University, 25240 Erzurum, Turkey

[3] Department of Chemistry, Koç University, 34450 İstanbul, Turkey

[4] Boreskov Institute of Catalysis, 630090 Novosibirsk, Russian Federation

[5] Interdisciplinary Nanoscience Center (iNANO) and Department of Chemistry, Aarhus University, Gustav Wieds Vej 14, 8000 Aarhus C, Denmark

[6] Aarhus Institute of Advanced Studies (AIAS), Aarhus University, Høegh-Guldbergs Gade 6B, 8000 Aarhus C, Denmark

photons of wavelength ≤460 nm [9]. This particularly advantageous electronic structure renders g-C_3N_4 as one of the few efficient photocatalytic semiconductors that can be activated with VIS light illumination constituting a major portion of the solar spectrum. Furthermore, uniquely versatile chemical composition and surface structure of g-C_3N_4 pave the way to diverse synthetic opportunities including surface functionalization, advanced nano/microstructure engineering, doping, deposition or coupling methods which can be exploited in order to obtain remarkable enhancement in the photocatalytic activity of g-C_3N_4-based family of materials. Among these synthetic opportunities, template-assisted methods are particularly beneficial as they enable fine-tuning of the surface, electronic, and morphological properties of g-C_3N_4 and also allow the design of porous structures [10–13]. Therefore, by exploiting such synthetic templating opportunities, mesoporous or microporous photocatalytic structures with a large surface area can be synthesized which in turn, may increase the number of exposed active sites of the photocatalyst, enhance VIS light absorption and improve photocatalytic activity.

In the current study, a cost-effective and a facile synthetic method utilizing the thermal polycondensation of guanidine hydrochloride (GndCl) precursor in the presence of a silica template was used to obtain mesoporous g-C_3N_4 (mpg-C_3N_4) materials. This is followed by a detailed structural characterization of the synthesized materials using a multitude of analytical techniques. In the light of these detailed characterization efforts, relative photocatalytic activity of the synthesized family of mpg-C_3N_4 materials in the photodegradation of multiple organic pollutants-namely, rhodamine B (RhB), methyl orange (MO), bromocresol purple (BCP), and methylene blue (MB)- were investigated under visible (VIS) and ultraviolet (UV) light irradiation and compared to that of a commercial Degussa P25 benchmark catalyst.

2 Experimental

2.1 Synthesis of the mpg-C_3N_4

mpg-C_3N_4 materials used in the current work were prepared from the thermal polycondensation of GndCl in the presence of Ludox® HS40 colloidal silica as the template [14]. In this method, mpg-C_3N_4 structure was acquired after an etching process [14] and the mesoporosity of the resulting material was verified by the measured BET specific surface area (SSA) of 200 m^2 g^{-1}. In the currently used synthetic protocol, 4.0 g of GndCl (for molecular biology, ≥99 %, Sigma-Aldrich) was dissolved in 4 mL distilled water in a glass vial and added dropwise into 10 g of Ludox® HS40 colloidal silica (SiO_2, 40 wt% suspension in H_2O, Sigma-Aldrich) under vigorous stirring. The resultant mixture was heated at 50 °C and continuously stirred during which the reaction was allowed to proceed for 12 h. After cooling to room temperature, obtained white solid was crushed in a ceramic mortar and was placed into a quartz crucible with a cover for annealing. The crucible was heated to 550 °C with a ramp rate of 4–5 °C min^{-1} under Ar(g) flow and kept at this temperature for 2 h in a horizontal quartz-tube oven. As an alternative material, another mpg-C_3N_4 sample was prepared using the same procedure, where the final annealing step was performed at 600 °C for 2.5 h. Next, the yellow solid powders attained via these two similar protocols were reacted with 4 M, 200 mL of ammonium hydrogen difluoride (NH_4HF_2, 95 % Sigma-Aldrich) solution for 2 days to remove the silica template. Finally, obtained powders were repeatedly washed with water and ethanol subsequently in order to remove the residual reactants and were dried overnight at ca. 50 °C in a vacuum oven. Resulting samples are named as mpg-C_3N_4-550 and mpg-C_3N_4-600 in the current text.

2.2 Structural Characterization

Crystal structures of the synthesized materials were determined via a Rigaku Miniflex X-ray diffractometer (XRD) equipped with Cu Kα radiation with λ = 1.54 Å, operated at 30 kV and 15 mA. XRD patterns were recorded in the 2θ range of 10–80° with a step width of 0.02° and a scan rate of 1.4° min^{-1}.

Fourier transform-infrared (FTIR) spectra were collected using a Bruker Tensor 27 spectrometer in the frequency range of 400–4000 cm^{-1} after preparing pellets of the synthesized powder materials via physical mixing with KBr(s).

X-Ray photoelectron spectroscopy (XPS) measurements were performed via a SPECS XP spectrometer (Germany) equipped with a PHOIBOS hemispherical energy analyser. A monochromatic Al $K\alpha$ X-ray excitation (hv = 1486.74 eV, 350 W) source was employed in the XPS data acquisition. Binding energy (BE) calibration of the XP spectra were carried out with the help of the amorphous carbon C*1 s* signal located at 284.6 eV [15].

The Brunauer-Emmett-Teller (BET) SSA measurements of the synthesized catalysts were determined by nitrogen adsorption–desorption isotherms using a Micromeritics Tristar 3000 surface area and pore size analyzer. Prior to SSA analysis, all samples were outgassed in vacuum for 2 h at 150°C. Also, pore size distributions of the materials were obtained by using the Barrett-Joyner-Halenda (BJH) method.

Solid-state Magic Angle Spinning (MAS) NMR experiments were performed at a 500 MHz Avance II Bruker

NMR spectrometer. The ^{13}C and ^{15}N CPMAS spectra of the mpg-C_3N_4-550 and mpg-C_3N_4-600 samples were recorded by using a 4 mm triple resonance probe at 8 kHz MAS and room temperature. The cross-polarization (CP) experiments were set up with a ramp on proton channel, and the acquisitions were done under proton decoupling. 1 s of recycle delay was used for the ^{13}C and ^{15}N experiments with 1024–4096 scans, respectively. The chemical shifts were referenced externally to liquid ammonia at 0 ppm for ^{15}N chemical shifts, and by using adamantine at 38.48 ppm for the ^{13}C chemical shifts.

Ultraviolet and visible (UV–Vis) absorption spectra of the investigated materials were recorded via a Varian Carry 300 UV–Vis double beam spectrophotometer with a 600 nm min^{-1} scan rate and 1 nm data interval over a wavelength range of 200–800 nm.

2.3 Photocatalytic Activity Measurements

Photocatalytic activities of the materials were investigated by photodegradation of ubiquitous model organic pollutants representing a variety chromophores [6–8, 16–20]. Along these lines, rhodamine B (RhB), methyl orange (MO), bromocresol purple (BCP), and methylene blue (MB) dyes were selected (Scheme 1). These dyes possess various chemical functional groups and enable the assessment of the activity of the currently synthesized photocatalytic architectures under UV and VIS illumination against different categories of organic dyes, namely rhodamine, azo, triarylmethane, and thiazine dyes; respectively [21]. For each of the model pollutants used in the current study, a concentration versus absorption (*i.e.* a calibration) curve was prepared in order to quantify the concentration of the model pollutants during the photodegradation process. Concentration ranges corresponding to the linear regimes of the calibration curves were utilized in the quantification studies. Furthermore, all of the photocatalytic activity results were benchmarked with respect to the commercial reference photocatalyst, Degussa P25 (Sigma-Aldrich).

In a typical photocatalytic degradation experiment [3, 4], a suspension of mpg-C_3N_4 powder in deionized water was prepared. After sonication of the prepared aqueous suspension for 20 min, an appropriate amount of dye (RhB, MO, BCP or MB) from its 60 mg L^{-1} stock solution was added to the mixture in order to have a final dye concentration of 10 mg L^{-1}. 8 mL (for UV studies) or 6 mL (for VIS studies) portions of these dye solutions were used during the photodegradation studies where final volume of the solutions were 48 mL (for UV studies) and 36 mL (for VIS studies). Before starting each degradation experiment, a 3 mL aliquot was collected immediately in order to calculate the initial dye concentration in the mixture. This is followed by the placement of the suspension in a home-made photocatalytic reactor. In order to monitor photocatalytic performances of the g-C_3N_4 samples under UV or VIS irradiation, two different reactors were utilized. Photocatalytic activity measurement cells were equipped with UV or VIS irradiation sources, air-cooling fans for temperature control and stirrers for continuous stirring. For the UV photocatalytic activity measurements, a Sylvania UV-lamp (F8 W, T5, Black-light, 8 W, 368 nm), while for the VIS photocatalytic activity measurements an Osram 35 W high intensity discharge lamp (metal halide lamp with ceramic burner, HCI-TC 35 W/942 NDL PB, 2000 μmol m^{-2} s^{-1} in 400–700 nm range) were used as the corresponding irradiation sources. Next, the suspension containing the dye and the photocatalyst was stirred under dark conditions at room temperature for 60 min in order to reach the adsorption–desorption equilibrium. This dark period is critical for the elimination of measurement errors caused by the dye adsorption on the photocatalyst surface. Next, the suspension was continuously stirred (500 rpm) and irradiated under UV or VIS irradiation sources. Then, aliquots (3 mL each) from the irradiated suspension were extracted after various time intervals. These aliquots were centrifuged with a rate of 6000 rpm for 30 min, and the visible absorption spectra of the decant were obtained to calculate the remaining concentration of the dye in the suspension after a given duration of irradiation. For the calculation of

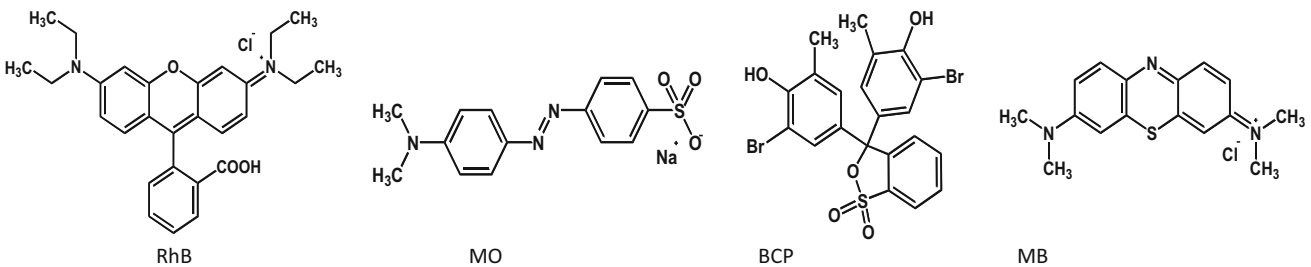

Scheme 1 Molecular structures of the selected organic dye compounds (*i.e.* model pollutants) for monitoring the photodegradation performance of the prepared photocatalysts

the concentrations via UV–Vis measurements, calibration curve for each dye ($R^2 = 0.9991$ for RhB, $R^2 = 0.9996$ for MO, $R^2 = 0.9981$ for BCP, and $R^2 = 0.9992$ for MB dyes) were obtained, where the intensities of the dye absorption signal at a fixed wavelength (553, 451, 429 and 670 nm for RhB, MO, BCP, and MB dyes; respectively) were recorded as a function of known dye concentrations. Furthermore, similar control (*i.e.* blank) experiments using identical light sources and identical experimental conditions in the absence of a photocatalyst were also performed in order to measure the photochemical (*i.e.* non-photocatalytic) self-degradation of the dyes in a quantitative manner. These latter values were used as the baseline in the quantification of the photocatalytic degradation studies.

Rate of photocatalytic degradation, r, could be expressed by the Langmuir–Hinshelwood (L–H) model [22]:

$$r = -\frac{\mathrm{dC}}{\mathrm{dt}} = \frac{kKC}{1 + KC} \quad (1)$$

where k is the reaction rate constant, C is the dye concentration and K is the adsorption equilibrium constant. When the dye concentration is very small, this equation becomes:

$$r = -\frac{\mathrm{dC}}{\mathrm{dt}} \approx kKC = k_{app}C \quad (2)$$

where $kK = k_{app}$ (k_{app}, apparent rate constant) and thus the rate of degradation obeys *pseudo* first order kinetics. Hence, the *pseudo* first order apparent rate constant (min^{-1}) for degradation, k_{app}, can be obtained from *Eq.* 3:

$$\ln\frac{C}{C_0} = -k_{app}t \quad (3)$$

where, C_0 is the initial concentration and C is the concentration at a given time (t) of the dye. Then, k_{app} can be derived from a plot of $ln(C/C_0)$ versus t.

3 Results and Discussion

3.1 Characterization of the Synthesized mpg-C_3N_4 Samples

In order to establish correlations between the photocatalytic activity of the synthesized photocatalysts and their structural properties, as-prepared mpg-C_3N_4 samples were characterized in detail by using XRD, FT-IR, XPS, BET and solid-state MAS NMR techniques. Figure 1a presents the XRD patterns of the mpg-C_3N_4-550 and mpg-C_3N_4-600 samples revealing typical major diffraction peaks at $2\theta = 27.5°$ and $2\theta = 27.6°$; respectively. These strong diffraction peaks can be readily assigned to (002) diffraction planes (JCPDS 87-1526) of g-C_3N_4 corresponding to the characteristic interplanar stacking structure of the conjugated aromatic system [12, 23–25]. Using this information, interlayer stacking distance (d_1) for mpg-C_3N_4-550 and mpg-C_3N_4-600 samples can be calculated as 0.324 nm 0.323 nm; respectively (Scheme 2). These interlayer stacking distances are slightly smaller than that of the crystalline graphite (d = 0.353 nm) [11] and crystalline g-C_3N_4 (d = 0.340 nm) [26] suggesting the presence of a higher packing density for mpg-C_3N_4-550 and mpg-C_3N_4-600. It is rather difficult to detect the relatively minor g-C_3N_4 characteristic diffraction peak ($2\theta = 13.2°$, associated with d_2 in Scheme 2) due to the (100) planes corresponding to intralayer/in-plane diffraction signals for mpg-C_3N_4-550 sample (Fig. 1a, inset); while this peak is readily visible for mpg-C_3N_4-600. Lack of this latter minor diffraction signal was also reported in the literature for relatively disordered mesoporous g-C_3N_4 samples prepared by hard templates yielding a porous and a less-ordered microstructure [12, 25]. Using the $2\theta = 13.2°$ signal, a repeating distance of $d_2 = 0.675$ nm can be calculated which can be attributed to the in-plane structural repeating motifs (Scheme 2) of the aromatic system which is close to the related dimensions of a single tri-s-triazine unit (ca. 0.71–0.73 nm) [11, 23]. These observations are is in agreement with the formation of a g-C_3N_4 structure. When GndCl is heated directly in air between 500 and 650°C these two characteristic diffraction peaks for g-C_3N_4 sample appears simultaneously, while the intensity of the 13.0° peak increases, 27.3° peak shifts slightly to higher angles with the increasing temperature [9].

FTIR spectroscopy was also used to examine the vibrational characteristics and surface functional groups of the synthesized mpg-C_3N_4 samples (Fig. 1b). FTIR spectra corresponding to mpg-C_3N_4-550 and mpg-C_3N_4-600 samples exhibit rather similar features with broad and convoluted bands located at 3000–3500 cm^{-1} which can be ascribed to the N–H stretchings corresponding to the hydrogenation of the terminal nitrogen atoms in the mpg-C_3N_4 structure (Scheme 2) or N–H functionalities located at the surface defect sites. Furthermore, the weak shoulder at >3500 cm^{-1} can be associated with O–H stretchings originating from adsorbed water molecules on the mpg-C_3N_4 surface and/or hydroxyl functionalities on the terminal atoms or surface defects. IR absorption band at 1636 cm^{-1} in Fig. 1b can be ascribed to the C–N stretching modes, while four different strong vibrational features at 1247, 1315, 1423 and 1569 cm^{-1} correspond to the typical stretching modes of the C–N heterocycle [23, 27, 28]. The absorption band at 808 cm^{-1} can be attributed to the out-of-plane ring bending modes of C–N heterocycles. The sharp and relatively weaker band around 2180 cm^{-1} can be assigned to the –C≡N triple bond stretchings of cyano groups which are possibly formed at the defect sides or

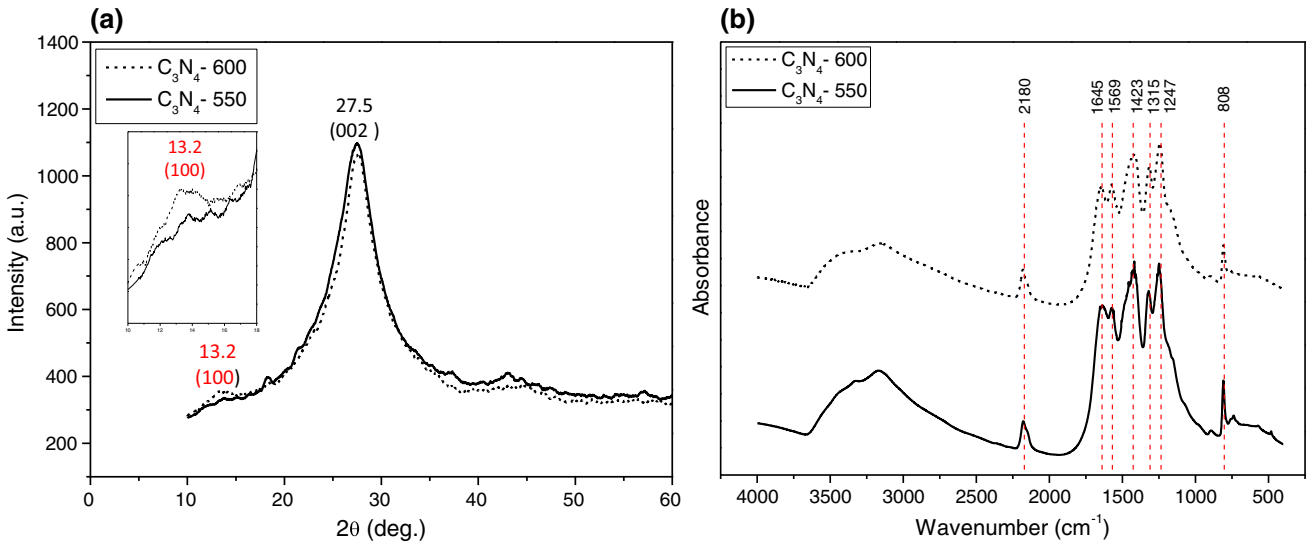

Fig. 1 **a** XRD patterns and **b** FTIR spectra of the mpg-C_3N_4-550 (*solid curves*) and mpg-C_3N_4-600 (*dotted curves*) samples

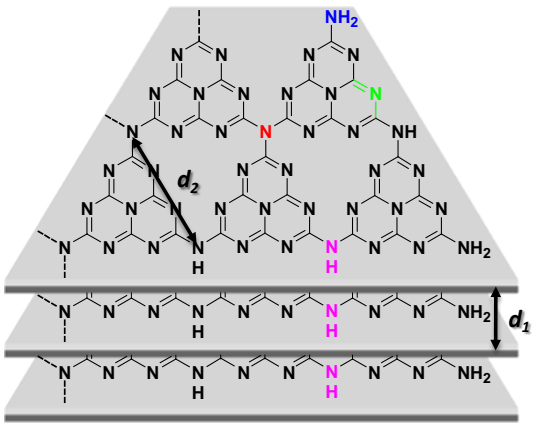

Scheme 2 Illustration of the stacked layers of mpg-C_3N_4. N atoms in various functionalities are color coded as: *blue* (sp^3-hybridized terminal amino group nitrogen, -C-NH_2), *green* (sp^2-hybridized s-triazine aromatic ring nitrogen, C=N–C), *red* (bridging/interlinking sp^3 hybridized nitrogen, N–(–C–)$_3$), and *pink* (sp^3-hybridized terminal amino group nitrogen, (–C–)$_2$–NH). (d_1; inter-layer and d_2; intralayer/in-plane distance)

located at less ordered (*i.e.* amorphous-like) C_xN_y minority domains which are produced during the synthesis process [26, 28, 29].

Surface chemistry and the functional groups existing on the mpg-C_3N_4 surfaces were also investigated by XPS measurements (Figs. 2 , S1). Corresponding XP survey spectra (Fig. S1 and Table 1) show that the mpg-C_3N_4-550 and mpg-C_3N_4-600 samples mainly include C and N elements with a relatively smaller contribution from O, along with minor F residues originating from the etching protocol used in the synthesis. As illustrated by the lack of any Si signals in the XPS survey scans given in Fig. S1, silica template used in the synthesis could be completely removed after the etching process.

C*1 s* region of the XP spectra of mpg-C_3N_4 (Fig. 2a) can be deconvoluted into four major features located at binding energy (B.E.) values of 284.6, 286.0, 288.3, and 289.7 eV which are labelled as C1, C2, C3, and C4 in Fig. 2a; respectively. As can be seen in Scheme 2, there exists two different prominent C-containing functionalities in the ideal structure of mpg-C_3N_4 (Scheme 2); both of which reveal themselves in the XPS results given in Fig. 2a. The most intense C*1 s* feature among these set of signals at 288.3 eV (*i.e.* C3) can be attributed to the sp^2-hybridized s-triazine aromatic ring carbon, (–N–)$_2$–C=N [30, 31]. The smaller C*1 s* signal located at 286.0 eV (*i.e.* C2) is assigned to sp^2-hybridized s-triazine aromatic ring carbon coordinated to the terminal amino group, N–C(–NH_2)=N [30, 32, 33]. Furthermore, C*1 s* feature labelled as C1 in these set of signals positioned at 284.6 eV is not likely to be associated with the mpg-C_3N_4 structure and can be ascribed to the C–C or C=C functionalities present in the graphite/amorphous carbon/$C_xN_yH_z$-like disordered minority domains [30, 34]. Finally a fourth C*1 s* feature (*i.e.* C4 in Fig. 2a) is also observed at 289.7 eV for the mpg-C_3N_4-600 sample which can be assigned to a group including a highly oxidized C species such as CO_3^{2-} [34]. Note that although vibrational spectroscopic signatures of these minor carbonate functionalities are expected to be observed within 1200–1500 cm^{-1} in the dotted FT-IR spectrum presented Fig. 1b, they are not readily discernible in Fig. 1b. It is highly probable that these minor vibrational features are strongly overwhelmed by the intense mpg-C_3N_4 features overlapping with the carbonate IR bands appearing in this frequency region.

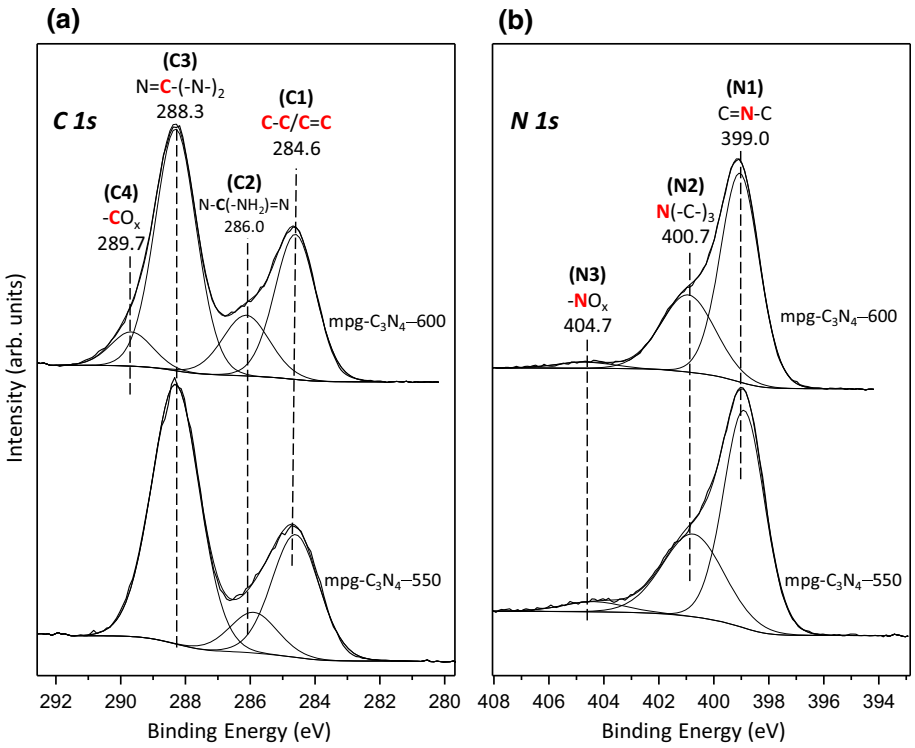

Fig. 2 Normalized XPS data for the **a** C*1 s* region and **b** N*1 s* region of mpg-C_3N_4-550 (*bottom*) and mpg-C_3N_4-600 (*top*) samples

Table 1 Surface atomic composition analysis of mpg-C_3N_4-550 and mpg-C_3N_4-600 obtained via current XPS results

	Carbon				Nitrogen			Oxygen	Fluorine
mpg-C_3N_4-550	C–C (C1)	N–C(–NH2)=N (C2)	N=C–(–N–)$_2$ (C3)	CO_x (C4)	C=N–C (N1)	N(–C–)$_3$ (N2)	NO_x (N3)		
Peak position	284.6	285.9	288.3	–	398.9	400.5	404.7	532.9	687.1
FWHM	1.72	1.74	1.72	–	1.76	2.6	2.6	3.29	3.62
At. % conc.	14.4	4.8	30.7		27.8	15.6	1.9	3.2	1.7
mpg-C_3N_4-600	C–C (C1)	N–C(–NH2)=N (C2)	N = C–(–N–)$_2$ (C3)	CO_x (C4)	C=N–C (N1)	N(–C–)$_3$ (N2)	NO_x (N3)		
Peak position	284.6	286.1	288.3	289.7	399.1	400.9	404.7	533.0	–
FWHM	1.50	1.70	1.50	1.50	1.66	2.31	2.31	3.25	–
At. % conc.	15.9	7.6	26.5	3.8	27.2	13.9	1.1	4.0	–

N*1 s* region of the XPS data for mpg-C_3N_4-550 and mpg-C_3N_4-600 samples given in Fig. 2b reveal three distinct N*1 s* states located at 399, 400.7, and 404.7 eV which are labelled as N1, N2, and N3 in Fig. 2b; respectively. The most intense N*1 s* feature at 399.0 eV (*i.e.* N1) in Fig. 2b can be assigned to the sp^2-hybridized s-triazine aromatic ring nitrogen, C=N–C [30, 35]. On the other hand, the second mpg-C_3N_4-related N*1 s* deconvolution feature in Fig. 2b appears at 400.7 eV (*i.e.* N2) which can be attributed to the bridging/interlinking sp^2-hybridized nitrogen connecting s-triazine rings, N(–C–)$_3$ [30, 36]. It should be considered that there may be multiple types of interlinking nitrogen species connecting the s-triazine rings such as the N atom inside a single *tri*-s-triazine group or an N-atom connecting three different *tri*-s-triazine groups. Note that relatively minor N*1 s* signal associated with the sp_3-hybridized terminal amino group nitrogen species (–C–NH_2) in the mpg-C_3N_4 structure is also possibly overlapping with the more dominant N(–C–)$_3$ signal labelled as N2 in Fig. 2b [30, 36]. Therefore, as can be seen in Fig. 2b and Table 1, it is reasonable to observe a broader FWHM value for the N2 feature. Remaining mpg-C_3N_4-related N*1 s* feature (labelled as N3 in Fig. 2b) located at 404.7 eV is likely to arise from –NO_x functionalities due to contamination.

XPS analysis of the mpg-C_3N_4-600 sample (Fig. 2a, b top spectra) reveals some similarities to that of the mpg-C_3N_4-550 sample such as the presence of C1–C3 and N1–N3 signals in both samples; while significant spectral differences between these two samples can also be readily recognized. These dissimilarities can be analyzed in more depth by calculating the relative percent surface atom (%At.) concentrations (Table 1) for these two samples, which can be obtained by normalizing the integrated XPS signals for different C*1 s* and N*1 s* states with their corresponding photoemission cross-section factors. These results indicate that increasing the polycondensation temperature used in the synthetic protocol from 550 to 600 °C leads to a visible decrease in the relative At. % values of C3 (*i.e.* C atoms inside the s-triazine rings of mpg-C_3N_4, (–N–)$_2$–C=N) and N2 (*i.e.* bridging/interlinking nitrogen connecting s-triazine rings, N(–C–)$_3$C) signals, along with a less significant but a detectable decrease in the N1 At. % value originating from s-triazine aromatic ring nitrogen, C=N–C. Moreover, at 600 °C, the relative At. % value of the C1 signal due to C–C or C=C functionalities present in the graphite/amorphous carbon/$C_xN_yH_z$-like disordered minority domains also increases.

These observations suggest that at 600 °C, interlinks between s-triazine rings in the mpg-C_3N_4 2D-structure are partially disconnected to form smaller patches/islands of mpg-C_3N_4. Furthermore, it is apparent that this higher synthesis temperature also results in the cleavage of (–N–)$_2$–C=N linkages inside the s-triazine rings of the mpg-C_3N_4 structure. Besides, it is likely that the higher synthesis temperature also increases the relative amount of s-triazine aromatic ring C atoms which are coordinated to terminal amino groups, N–C(–NH_2)=N. In other words, terminations of the mpg-C_3N_4 patches may become more defective at 600 °C and deviate more significantly from the ideal representation given in Scheme 2. In addition, the relative amount of graphite/amorphous carbon/$C_xN_yH_z$-like disordered minority domains increases at 600 °C. Complementary analysis of these structural findings suggest that increasing the synthesis temperature from 550 to 600 °C leads to partial breaking of the s-triazine interconnections and aromatic ring opening which in turn results in the formation of defective and smaller 2D islands of s-triazine groups which also co-exist with an increasing amount of graphite/amorphous carbon/$C_xN_yH_z$-like disordered domains.

It is worth mentioning that although XPS data discussed in the light of the results given in Fig. 2 and Table 1 suggest that mpg-C_3N_4-600 sample exhibits important structural variations and a more defective nature than that of the mpg-C_3N_4-550 sample; both of these samples can still be predominantly characterized as mpg-C_3N_4-600 sample. This becomes more clear when the total C*1 s* percent surface atomic concentration (At. %) values (*i.e.* At. % (C3) + At. % (C2) given in Table 1) originating from the mpg-C_3N_4 structure is compared to that of the N*1 s* At. % values originating from the mpg-C_3N_4 structure (*i.e.* At. % (N1) + At. % (N2) given in Table 1). It is clear that the stoichiometry of the ideal mpg-C_3N_4 structure implies a C/N atom ratio of ca. 0.75. Calculation of the following C/N atom ratio via XPS data given in Table 1:

$$C/N = \frac{\%\ \text{At.(C3)} + \%\ \text{At.(C2)}}{\%\ \text{At.(N1)} + \%\ \text{At.(N2)}} \quad (4)$$

reveals a C/N atom ratio of ca. 0.8 for both mpg-C_3N_4-550 and mpg-C_3N_4-600 samples. This observation is in agreement with the fact that both samples are dominated by mpg-C_3N_4-structures as evident by the similar XRD (Fig. 1a) and FTIR (Fig. 1b) characteristics.

Specific surface area (SSA) values and the porosity of the mpg-C_3N_4-550 and mpg-C_3N_4-600 samples were also investigated in order to shed light on the structural differences between these two different photocatalysts. Typical N_2 adsorption–desorption isotherms and the corresponding pore size distribution curves for these samples are shown in Figs. 3a ,b; respectively. Based on the corresponding shapes of the curves, isotherms given in Fig. 3a can be identified as type-IV isotherms [9, 13, 14, 37, 38]. The hysteresis loop of the mpg-C_3N_4-550 can be classified as H2-type indicating the presence of "ink-bottle" (i.e. pores comprised of narrow necks and wide bodies) shaped mesopores [38]. In contrast, the hysteresis loop of the mpg-C_3N_4-600 material can be classified as H3-type revealing the existence of "plate-like particles" with "slit-shaped" mesopores [38].

SSA values of the mpg-C_3N_4-550 and mpg-C_3N_4-600 samples were determined via BET method and found to be 182 and 155 $m^2\ g^{-1}$; respectively. In agreement with the characterization results discussed above, high temperature synthesis carried out at 600 °C, results in the partial destruction of the ordered 2D/planar/layered structure of the mpg-C_3N_4 and leads to the agglomeration (*i.e.* clustering/sintering), defect formation and production of graphite/amorphous carbon/$C_xN_yH_z$-like secondary domains which in turn results in a decrease in the SSA as compared to that of 550 °C.

Pore diameter distributions (Fig. 3b) were also calculated using the Barrett-Joyner-Halenda (BJH) method where the modified Kelvin equation was utilized in order to relate the amount of adsorbate removed from the pores of the material to the size of the pores, as the relative pressure (P/P_0) is decreased from a high value to a lower value. Pore size distribution curves shown in Fig. 3b show that mpg-C_3N_4-550 material has a very narrow pore diameter distribution which can be characterized by the presence of primarily a single type of pore with an average pore size of

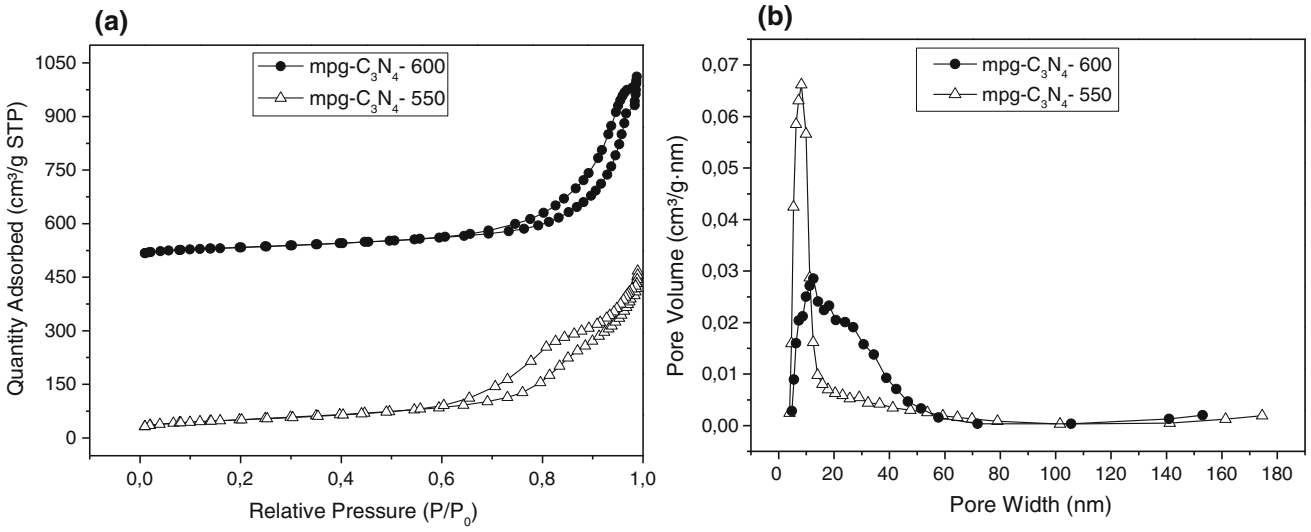

Fig. 3 **a** N_2 adsorption–desorption isotherms and **b** corresponding Barrett-Joyner-Halenda (BJH) pore-size distribution plots of mpg-C_3N_4-550 and mpg-C_3N_4-600

ca. 9 nm. On the other hand, pore-size distribution of the mpg-C_3N_4-600 material exhibits a bimodal character, revealing the presence of at least two different types of pores with average pore sizes of ca. 13 and 24 nm. In the light of the XPS results discussed above, it is likely that the former average pore size (13 nm) of the mpg-C_3N_4-600 sample can be associated with defective mpg-C_3N_4 patches with partially broken interlinking N–(–C_3–) functionalities where the second average pore size value may be due to the presence of a secondary graphite/amorphous carbon/$C_xN_yH_z$-like domains. Relatively lower specific surface area and the significantly broader pore size distribution (5–70 nm) of mpg-C_3N_4-600 with a bimodal character indicating the presence of both mesopores (2–50 nm) as well as a smaller number of macropores (>50 nm) is in good agreement with the co-existence of defective mpg-C_3N_4 domains together with the presence of graphite/amorphous carbon/$C_xN_yH_z$-like secondary domains [10, 39].

Since solid state MAS NMR is a powerful technique to identify chemical nature of solid materials [40–43], this technique was also utilized to further investigate mpg-C_3N_4-550 and mpg-C_3N_4-600 samples, as shown in Fig. 4a, b. Two prominent resonances were observed in the ^{13}C CPMAS spectra of the both of the mpg-C_3N_4 samples (Fig. 4a). The 157–164 ppm chemical shifts are indicative of two common carbon sites (–N–)$_2$–C=N and N–C(–NH_2)=N [44–48]. Besides these major signals, two other very low-intensity peaks located at ca. 151–171 ppm are also visible. These peaks can be tentatively attributed to the decomposed ring species. However, a multidimensional NMR investigation is required for the final assignment of these low-intensity peaks. Note that the resonance signals labelled with asterisk (*) in Fig. 4a are spinning side bands originating from the major signals.

The ^{15}N CPMAS spectra of the two samples are shown in Fig. 4b. The signals in these spectra are broader compared to resonances in typical melem or melamine spectra. This could indicate a structural heterogeneity in the studied samples with dissimilar chemical sites or different conformations. Although the low sensitivity of the CP NMR in the currently studied samples hampers the S/N, these results can still be evaluated in a qualitative manner. While mpg-C_3N_4-550 and mpg-C_3N_4-600 samples show quite similar ^{15}N CPMAS spectra, there exist noteworthy differences [44, 47]. Moreover, relative intensities of the resonances at ca. 110, 136, and 190 ppm differs slightly indicating the composition differences in the studied two materials. The intense chemical shift observed at ~136 ppm was reported to be a characteristic resonance of tri-s-triazine species [47]. Even though ^{15}N CPMAS chemical shifts observed in the spectra given in Fig. 4b resemble that of the pure melem and melamine, there exists differences in resonance shifts which can be associated to the chemical structure variations in the studied materials compared to the pure monomeric species due to different ring structures or different substitution of the functional groups at the terminal or ring sites [47, 48].

3.2 Photocatalytic Performance

Photocatalytic performance of the samples was evaluated by the photocatalytic dye (*i.e.* RhB, MO, BCP, and MB) degradation studies under UV and VIS light illumination as displayed in Figs. 5, 6, 7, S2. Furthermore, photodegradation experiments with a commercial Degussa P25

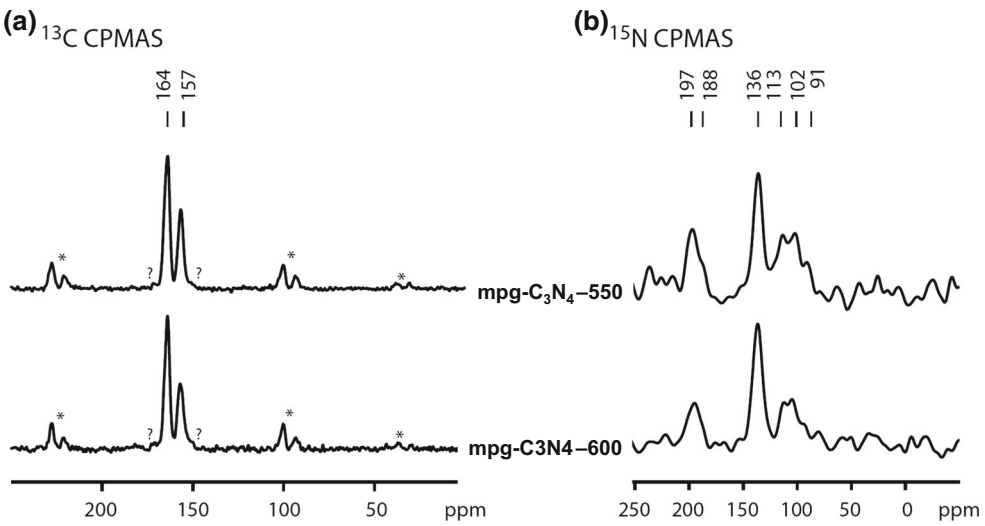

Fig. 4 Solid state ^{13}C and ^{15}N CPMAS spectra of mpg-C_3N_4-550 and mpg-C_3N_4-600 samples. The spectra were recorded at 500 MHz with a 4 mm triple resonance NMR probe at 8 kHz MAS and room temperature. The chemical shifts observed are given on top of the spectra

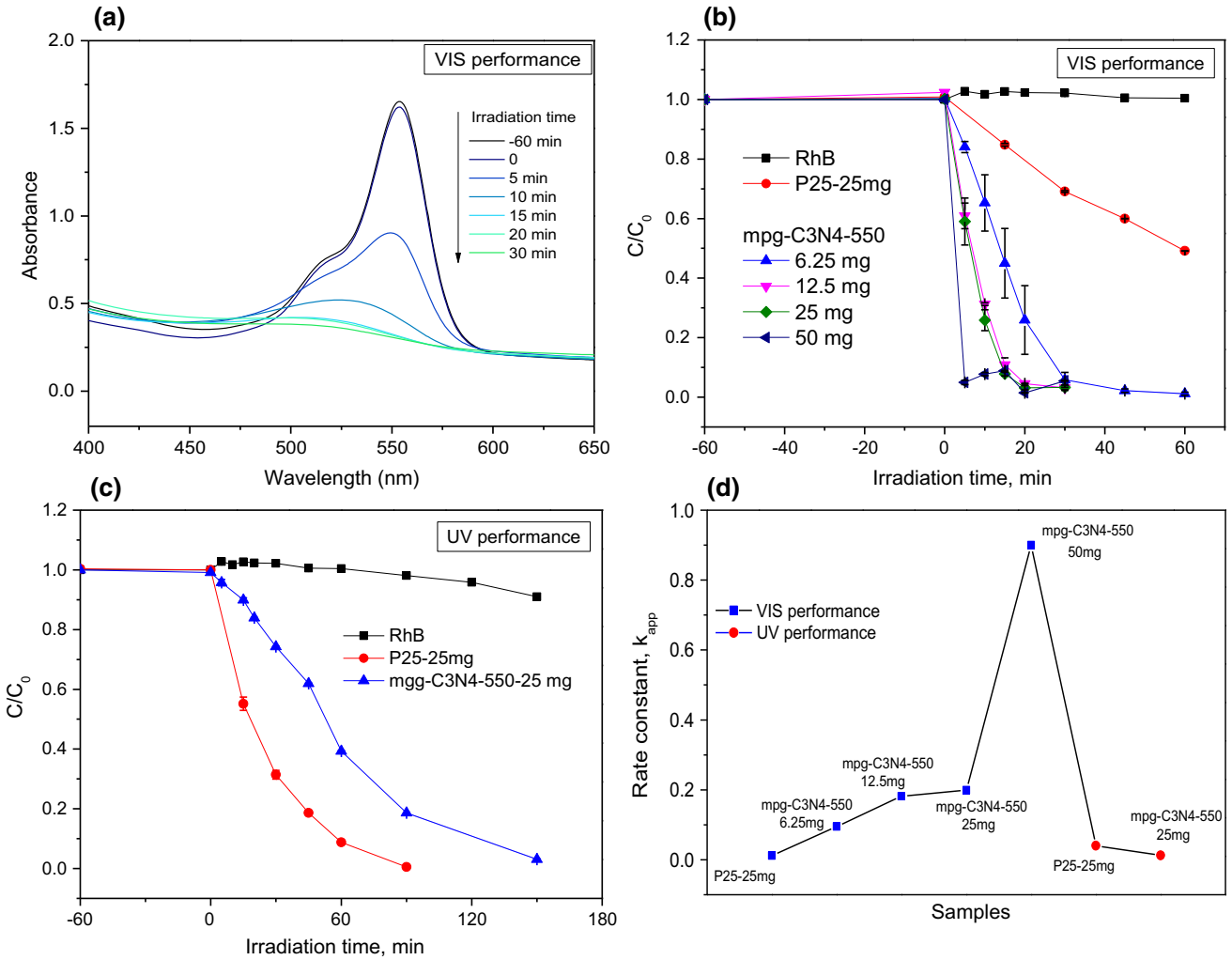

Fig. 5 **a** Variation of the absorption spectra of 10 mg L^{-1} RhB solutions as a function of VIS-light irradiation time in the presence of mpg-C_3N_4-550 (25 mg), **b** RhB photocatalytic degradation performance of mpg-C_3N_4-550 as a function of catalysts loading under VIS-light. **c** Comparison of the RhB decoloration performances of Degussa P25, mpg-C_3N_4-550 and a blank (*i.e.* catalyst-free) systems under UV illumination. **d** Apparent rate constants of the catalysts presented in *panels* (*a–c*)

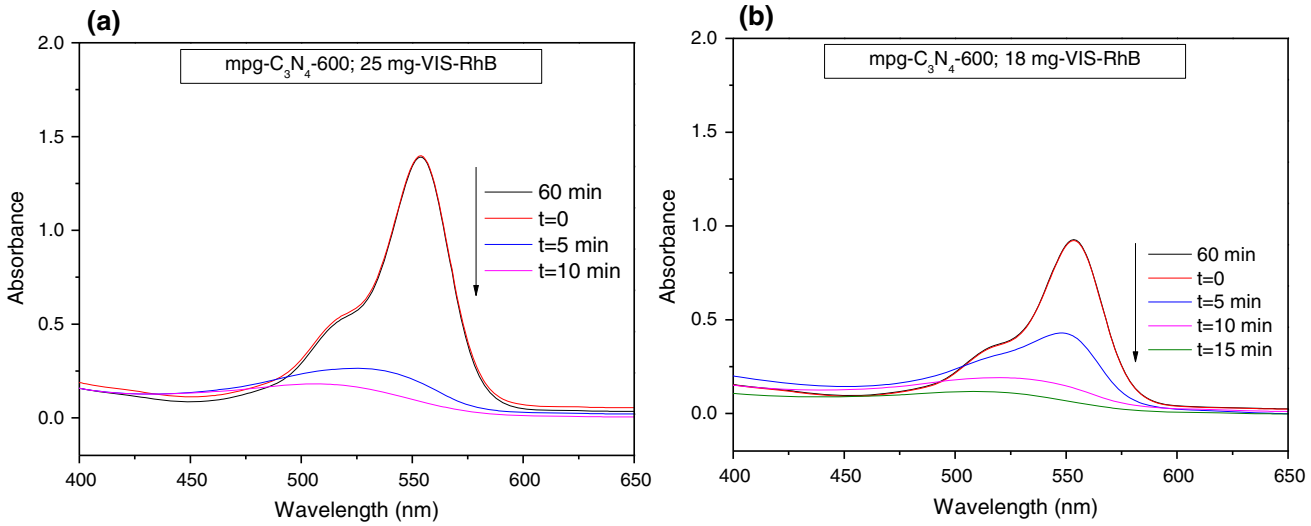

Fig. 6 Evolution of the UV–Vis absorption spectra of RhB solutions photodegraded using **a** 25 mg mpg-C_3N_4-600 and **b** 18 mg mpg-C_3N_4-600 photocatalyst under VIS-light irradiation

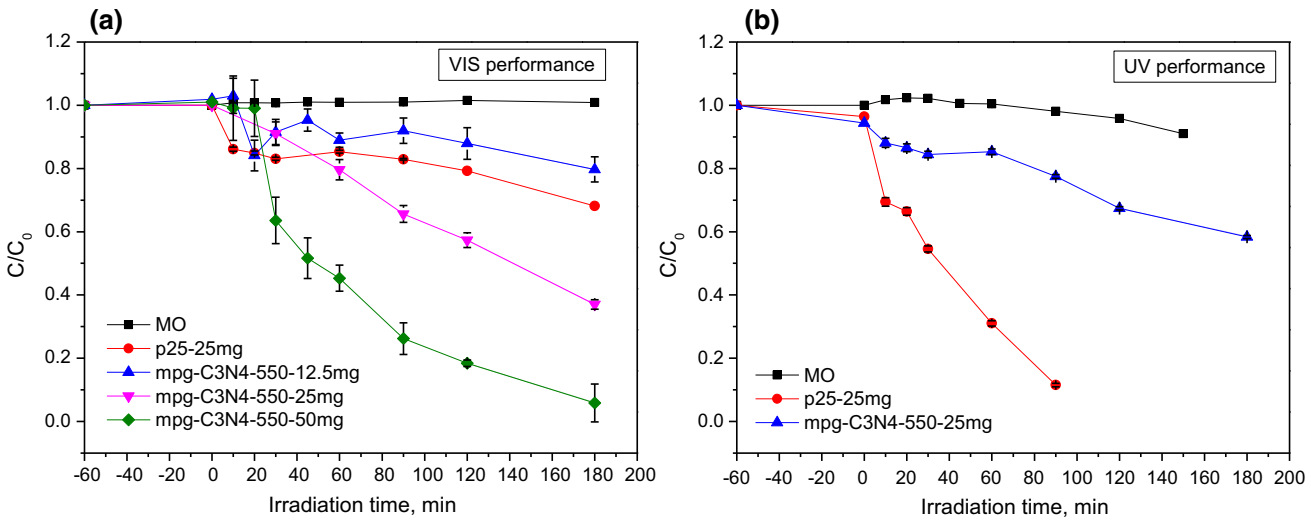

Fig. 7 Photodegradation performance results of mpg-C_3N_4-550 over 10 mg L^{-1} MO **a** under VIS-light irradiation as a function of catalyst loading and **b** under UV-light irradiation for 25 mg of mpg-C_3N_4-550. All of these measurements were also compared to similar measurements obtained with 25 mg of Degussa P25 benchmark catalyst under VIS or UV illumination

benchmark catalyst as well as additional control experiments in the absence of any catalysts were also performed. It must be noted that the degradation of RhB dye under VIS-light irradiation in the absence of a photocatalyst is negligible, however in the presence of UV light irradiation, a notable degradation was observed (Fig. 5b, c).

Since RhB is one of the most commonly used organic dye molecules in the former discoloration studies in the literature, it was selected as the model pollutant in order to determine the optimum catalyst loading under visible light irradiation. Currently synthesized mpg-C_3N_4-550 sample was chosen to compare the current photocatalytic activity results to other g-C_3N_4-550 materials formerly reported in the literature [14]. Typical variations in the absorption spectra of RhB after various durations of visible light irradiation in the presence of 25 mg of mpg-C_3N_4-550 is presented in Fig. 5a. Decoloration efficiency of the catalyst as a function of mpg-C_3N_4-550 loading was determined by calculating the decrease in the RhB concentration using the attenuation in the intensity of the absorption maximum of the dye solution (Fig. 5b). Figure 5b clearly shows that for all of the currently used mpg-C_3N_4-550 loadings, RhB degradation rate of mpg-C_3N_4-550 under VIS light greatly surpasses that of the Degussa P25 benchmark catalyst with

a huge margin. Figure 5 also illustrates that the photocatalytic degradation performance monotonically increases with the increasing catalyst loading. It should be emphasized that decoloration activity of the currently synthesized mpg-C_3N_4-550 sample is much higher than most of the corresponding literature studies, where g-C_3N_4 was synthesized via thermal polycondensation method using various precursors including GndCl [9, 49], melamine [13] and urea [50]. It is also worth mentioning that the decoloration of the RhB solutions with mpg-C_3N_4-550 demonstrated in Fig. 5a cannot be attributed to adsorption (*i.e.* a non-catalytic) process, since the RhB absorption signal intensity does not change under dark conditions during the first 60 min before the activation of the excitation source.

As the RhB degradation under VIS light in the presence of 50 mg of mpg-C_3N_4-550 is extremely fast, execution of the relatively slower (i.e. time consuming) sampling and spectroscopic characterization steps becomes experimentally challenging. In order to circumvent this practical difficulty and be able to collect a greater number of experimental data points for chemical kinetics analysis, a catalyst loading of 25 mg was utilized in the photocatalytic performance experiments presented in the rest of the text.

Photocatalytic activity of the mpg-C_3N_4-550 (25 mg) sample was also evaluated under UV-light irradiation ($\lambda = 368$ nm) in comparison to that of the commercial Degussa P25 benchmark catalyst (Fig. 5c). According to these results, mpg-C_3N_4-550 presents a lower RhB degradation performance than that of the Degussa P25 catalyst. These observations are in line with the relatively lower typical electronic band gap of g-C_3N_4 materials (*e.g.* 2.7 eV) rendering them more efficient photocatalysts under VIS-irradiation rather than UV-illumination (Fig. 5d).

Photocatalytic RhB degradation performance of mpg-C_3N_4 under VIS-light was also studied for samples which were prepared at 600 °C (i.e. mpg-C_3N_4-600). Figure 6a, b show the evolution of the absorption spectrum obtained during such studies for two different loadings (25 and 18 mg; respectively) of the mpg-C_3N_4-600 photocatalyst. The initial mpg-C_3N_4-600 catalyst loading (Fig. 6a, 25 mg) was preferred in order to be able to compare these results with that of the mpg-C_3N_4-550 sample (Fig. 5a, 25 mg) while the second loading (18 mg) enables the direct comparison of the currently synthesized mpg-C_3N_4-600 sample with an earlier study in the literature [9]. As shown in Fig. 6a, it is obvious that the main absorption band at around 553 nm almost completely disappears after 5 min of VIS light illumination of the RhB solution containing the mpg-C_3N_4-600 photocatalyst. In contrast, a similar extent of decoloration takes ca. 20 min for mpg-C_3N_4-550 (Fig. 5a). Considering the fact that mpg-C_3N_4-550 has a higher SSA value (182 m^2g^{-1}) than that of the mpg-C_3N_4-600 sample (155 m^2 g^{-1}), it is evident that the significantly higher photocatalytic decoloration activity of the latter catalyst cannot be directly correlated to its BET specific surface area but rather associated to its unique surface chemistry and functional groups.

It is worth emphasizing that the illumination power of the VIS-light source used in the current study (35 W) is almost an order of magnitude lower than that of the typical excitation sources used in comparable former studies (*e.g.* 300 W [5] and 500 W [33]) where mpg-C_3N_4 materials were synthesized via a GndCl precursor. In other words, currently synthesized mpg-C_3N_4-600 photocatalysts significantly surpasses the activity of the existing mpg-C_3N_4 photocatalysts in the literature. This is particularly evident when the attenuation of the RhB signal under 35 W VIS-light on 18 mg of the mpg-C_3N_4-600 photocatalyst is monitored over time (Fig. 5b) in comparison to a former study employing comparable RhB dye concentrations and comparable catalyst loadings [9] illuminated with 300 W VIS-light [9]. While Fig. 5b clearly shows that almost all of the RhB signal is lost in the first 10 min over mpg-C_3N_4-600, ca. 27 % of the RhB continues to survive on the mpg-C_3N_4 used in Ref. five even after 20 min of VIS light exposure [9].

On the other hand, the photocatalytic activity of the mpg-C_3N_4-550 sample was also studied in the photodegradation of other model organic dyes (MO, BCP, and MB) under both visible and UV light illumination. Figure 7a illustrates that currently synthesized mpg-C_3N_4 photocatalysts can also degrade dyes other than RhB having dissimilar chemical functional groups. Figure 7a suggests that for MO (10 mg L^{-1}) degradation under VIS-illumination, 25 mg mpg-C_3N_4-550 can outperform 25 mg Degussa P25 while under UV illumination this trend is reversed. Similar experiments performed with MB (data not shown) revealed that MB poisons all of the mpg-C_3N_4 catalysts revealing no detectable activity. Photocatalytic BCP degradation performance of mpg-C_3N_4-550 under UV and VIS-light results were also represented as supporting information in Fig. S2. It should be noted that 50 mg mpg-C_3N_4-550 sample presents a comparable BCP dye (10 mg L^{-1}) degradation performance under VIS-light irradiation to that of the 50 mg Degussa P25 catalyst. The lower activity of mpg-C_3N_4 catalysts towards the degradation of MB and BCP is most likely due to the strong adsorption of these dye molecules on the active sites of the photocatalyst in an irreversible manner, rendering the photocatalyst surface poisoned.

The reusability of the photocatalyst is an important factor for the practical applications targeting to the photodegradation of organic contaminants in water. Among all of the investigated samples mpg-C_3N_4-550 (25 mg) was selected to demonstrate the reusability performance for RhB, MO, and BCP dyes (Fig. 8) due to its slower kinetics

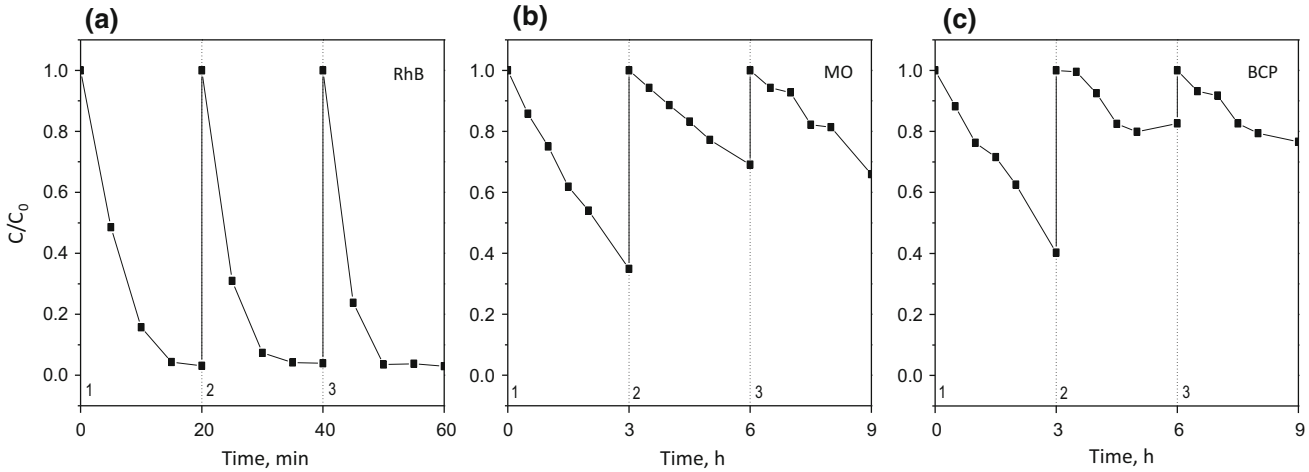

Fig. 8 Photocatalytic reusability cycles of mpg-C_3N_4-550 (25 mg) under visible light irradiation for **a** RhB, **b** MO, and **c** BCP. All of the initial dye concentrations in the prepared suspensions was identical (10 mgL^{-1})

than that of the more active mpg-C_3N_4-600 sample allowing the acquisition of a greater number of kinetic data points. For this purpose, by using the identical experimental conditions described above, photocatalytic performance studies were repeated for multiple successive catalytic runs. During these successive runs, photocatalysts were re-collected/isolated from the dye solutions after specific durations (i.e. after 20 min for RhB and after 3 h for MO and BCP) and directly used in the next catalytic run. It is observed that the mpg-C_3N_4-550 exhibits a stable RhB dye degradation performance without a significant loss of activity after three consecutive reaction cycles (Fig. 8a). However, photocatalytic efficiency decreases after the first measurement for MO and BCP dyes (Fig. 8b, c; respectively).

4 Conclusions

Mesoporous graphitic carbon nitride (mpg-C_3N_4) structures were synthesized by a facile template assisted method by utilizing the thermal polycondensation reaction of guanidine hydrochloride (guanidinium chloride, GndCl) at two different temperatures (*i.e.* 550–600 °C). Surface and structural properties of the synthesized mpg-C_3N_4 samples were characterized in detail via XRD, BET, FT-IR, XPS and solid-state MAS NMR. Currently synthesized mpg-C_3N_4 photocatalysts were found to be significantly active in the degradation of various model organic dye molecules such as rhodamine B (RhB), methyl orange (MO) and bromocresol purple (BCP) under low-power VIS light illumination surpassing former results in the literature. Enhanced activity of the currently synthesized mpg-C_3N_4-600 catalyst was attributed to its defective structure comprised of partial destruction of the interlinking-N functionalities connecting tri-s-triazine rings. In addition, this enhanced performance can also be associated to the partial removal of the interlinking N atoms inside the tri-s-triazine rings resulting in the formation of smaller 2D patches of defective and agglomerated mpg-C_3N_4 domains, synergistically co-existing with graphite/amorphous carbon/$C_xN_yH_z$-like secondary domains.

Acknowledgments This work was partially supported by Turkish Academy of Science Young Scientist program (TUBA-GEBIP). EIV acknowledges financial support from the Scientific and Technological Research Council of Turkey (TÜBİTAK, Program Code: 2221). MS acknowledges TÜBİTAK National Scholarship Program for PhD students for financial support. ÜA acknowledges financial support from DFF Mobilex grant and AIAS-COFUND fellowship.

References

1. Soylu AM, Polat M, Erdogan DA et al (2014) TiO2–Al2O3 binary mixed oxide surfaces for photocatalytic NOx abatement. Appl Surf Sci 318:16–21
2. Polat M, Soylu AM, Erdogan DA et al (2014) Influence of the sol–gel preparation method on the photocatalytic NO oxidation performance of TiO2/Al2O3 binary oxides. Catal Today 241:1–8
3. Erdogan DA, Solouki T, Ozensoy E (2015) A versatile bio-inspired material platform for catalytic applications: micron-sized "buckyball-shaped" TiO_2 structures. RSC Adv 5:47174–47182
4. Erdogan DA, Polat M, Garifullin R et al (2014) Thermal evolution of structure and photocatalytic activity in polymer microsphere templated TiO_2 microbowls. Appl Surf Sci 308:50–57
5. Zhao Z, Sun Y, Dong F (2015) Graphitic carbon nitride based nanocomposites: a review. Nanoscale 7:15–37
6. Fu D, Han G, Liu F et al (2014) Visible-light enhancement of methylene blue photodegradation by graphitic carbon nitride-titania composites. Mater Sci Semicond Process 27:966–974
7. Luo J, Zhou X, Ma L, Xu X (2015) Enhancing visible-light photocatalytic activity of g-C 3 N 4 by doping phosphorus and

coupling with CeO_2 for the degradation of methyl orange under visible light irradiation. RSC Adv 5:68728–68735
8. Niu P, Yin L-C, Yang Y-Q et al (2014) Increasing the visible light absorption of graphitic carbon nitride (melon) photocatalysts by homogeneous self-modification with nitrogen vacancies. Adv Mater 26:8046–8052
9. Shi L, Liang L, Wang F et al (2014) Polycondensation of guanidine hydrochloride into a graphitic carbon nitride semiconductor with a large surface area as a visible light photocatalyst. Catal Sci Technol 4:3235
10. Zhang F, Sun D, Yu C et al (2015) A sol–gel route to synthesize SiO_2/TiO 2 well-ordered nanocrystalline mesoporous photocatalysts through ionic liquid control. New J Chem 39:3065–3070
11. Dai H, Gao X, Liu E et al (2013) Synthesis and characterization of graphitic carbon nitride sub-microspheres using microwave method under mild condition. Diam Relat Mater 38:109–117
12. Groenewolt M, Antonietti M (2005) Synthesis of g-C3N4 nanoparticles in mesoporous silica host matrices. Adv Mater 17:1789–1792
13. Shi L, Liang L, Wang F et al (2015) In-situ bubble template promoted facile preparation of porous g-C3N4 with excellent visible-light photocatalytic performance. RSC Adv 5:63264–63270
14. Xu J, Wu H-T, Wang X et al (2013) A new and environmentally benign precursor for the synthesis of mesoporous g-C3N4 with tunable surface area. Phys Chem Chem Phys 15:4510
15. Moulder JF (1992) Handbook of X-ray Photoelectron Spectroscopy: A Reference Book of Standard Spectra for Identification and Interpretation of XPS Data. Perkin-Elmer Corporation, Physical Electronics Division
16. Li G, Yang N, Wang W, Zhang WF (2009) Synthesis, photophysical and photocatalytic Properties of N-doped sodium niobate sensitized by carbon nitride. J Phys Chem C 113:14829–14833
17. Lan Y, Qian X, Zhao C et al (2013) High performance visible light driven photocatalysts silver halides and graphitic carbon nitride (X = Cl, Br, I) nanocomposites. J Colloid Interface Sci 395:75–80
18. Li H, Liu Y, Gao X et al (2015) Facile synthesis and enhanced visible-light photocatalysis of graphitic carbon nitride composite semiconductors. Chem Sus Chem 8:1189–1196
19. Shi W, Guo F, Chen J et al (2014) Hydrothermal synthesis of InVO4/Graphitic carbon nitride heterojunctions and excellent visible-light-driven photocatalytic performance for rhodamine B. J Alloys Compd 612:143–148
20. Zhou Y, Zhang L, Liu J et al (2015) Brand new P-doped g-C 3 N 4: enhanced photocatalytic activity for H 2 evolution and Rhodamine B degradation under visible light. J Mater Chem A 3:3862–3867
21. Hunger K (2003) Industrial Dyes: Chemistry, Properties, Application. Wiley, Weinheim
22. Kumar KV, Porkodi K, Rocha F (2008) Langmuir-Hinshelwood kinetics – A theoretical study. Catal Commun 9:82–84
23. Yan SC, Li ZS, Zou ZG (2009) Photodegradation performance of g-C3N4 fabricated by directly heating melamine. Langmuir 25:10397–10401
24. Ge L, Han C, Liu J (2011) Novel visible light-induced g-C3N4/Bi2WO6 composite photocatalysts for efficient degradation of methyl orange. Appl Catal B Environ 108–109:100–107
25. Li H-J, Sun B-W, Sui L et al (2015) Preparation of water-dispersible porous g-C 3 N 4 with improved photocatalytic activity by chemical oxidation. Phys Chem Chem Phys 17:3309–3315
26. Zhang Y, Zhao H, Hu Z, et al. (2015) Protic Salts of High Nitrogen Content as Versatile Precursors for Graphitic Carbon Nitride: Anion Effect on the Structure, Properties, and Photocatalytic Activity. Chempluschem Ahead of Print
27. Zhou S, Liu Y, Li J et al (2014) Facile in situ synthesis of graphitic carbon nitride (g-C3N4)-N-TiO_2 heterojunction as an efficient photocatalyst for the selective photoreduction of CO_2 to CO. Appl Catal B Environ 158–159:20–29
28. Shen C, Chen C, Wen T et al (2015) Superior adsorption capacity of g-C_3N_4 for heavy metal ions from aqueous solutions. J Colloid Interface Sci 456:7–14
29. Miller DR, Holst JR, Gillan EG (2007) Nitrogen-rich carbon nitride network materials via the thermal decomposition of 2,5,8-triazido-s-heptazine. Inorg Chem 46:2767–2774
30. Yuan Y, Zhang L, Xing J et al (2015) High-yield synthesis and optical properties of g-C 3 N 4. Nanoscale 7:12343–12350
31. Xu H, Yan J, She X et al (2014) Graphene-analogue carbon nitride: novel exfoliation synthesis and its application in photocatalysis and photoelectrochemical selective detection of trace amount of Cu^{2+}. Nanoscale 6:1406–1415
32. Khabashesku VN, Zimmerman JL, Margrave JL (2000) Powder Synthesis and Characterization of Amorphous Carbon Nitride. Carbon N Y 12:3264–3270
33. Ronning C, Feldermann H, Merk R et al (1998) Carbon nitride deposited using energetic species: a review on XPS studies. Phys Rev B 58:2207–2215
34. Moulder John F (1992) Handbook of X-ray photoelectron spectroscopy: a reference book of standard spectra for identification and interpretation of xps data. Perkin-Elmer Corp, Physical Electronics Division
35. Li Y, Zhang J, Wang Q et al (2010) Nitrogen-rich carbon nitride hollow vessels: synthesis, characterization, and their properties. J Phys Chem B 114:9429–9434
36. Li Y, Xu S, Li H, Luo W (1998) Polycrystalline carbon nitride β-C3N4 films synthesized by radio frequency magnetron sputtering. J Mater Sci Lett 7:31–35
37. Gu Q, Gao Z, Zhao H et al (2015) Temperature-controlled morphology evolution of graphitic carbon nitride nanostructures and their photocatalytic activities under visible light. RSC Adv 5:49317–49325
38. Sing KSW (1985) Reporting physisorption data for gas/solid systems with special reference to the determination of surface area and porosity (Recommendations 1984). Pure Appl Chem 57:603–619
39. Chen R, Yu J, Xiao W (2013) Hierarchically porous MnO_2 microspheres with enhanced adsorption performance. J Mater Chem A 1:11682
40. Demir MM, Koynov K, Akbey Ü, Bubeck C, Park I, Lieberwirth I, Wegner G (2007) Optical properties of composites of PMMA and surface-modified zincite nanoparticles. Macromolecules 40:1089–1100
41. Akbey Ü, Graf R, Chu PP, Spiess HW (2009) Anhydrous Poly (2, 5-benzimidazole)–Poly (vinylphosphonic Acid) Acid-Base Polymer Blends: a Detailed Solid-State NMR Investigation. Aust J Chem 62:848–856
42. Akbey U, Granados-Focil S, Coughlin EB, Graf R, Spiess HW (2009) 1H solid-state NMR investigation of structure and dynamics of anhydrous proton conducting triazole-functionalized siloxane polymers. J Phys Chem B 113:9151–9160
43. Çelik SÜ, Coşgun S, Akbey Ü, Bozkurt A (2012) Synthesis and proton conductivity studies of azole functional organic electrolytes. Ionics 18:101–107
44. Wang XL, Fang WQ, Wang HF, Zhang H, Zhao H, Yao Y, Yang HG (2013) Surface hydrogen bonding can enhance photocatalytic H_2 evolution efficiency. J Mater Chem A 1:14089–14096
45. Dontsova D, Pronkin S, Wehle M, Chen Z, Fettkenhauer C, Clavel G, Antonietti M (2015) Triazoles: a new class of precursors for the synthesis of negatively charged carbon nitride derivatives. Chem Mater 27:5170–5179

46. Sehnert J, Baerwinkel K, Senker J (2007) Ab initio calculation of solid-state NMR spectra for different triazine and heptazine based structure proposals of g-C3N4. J Phys Chem B 111:10671–10680
47. Jürgens B, Irran E, Senker J, Kroll P, Müller H, Schnick W (2003) Melem (2, 5, 8-triamino-tri-s-triazine), an important intermediate during condensation of melamine rings to graphitic carbon nitride: synthesis, structure determination by X-ray powder diffractometry, solid-state NMR, and theoretical studies. J Am Chem Soc 125:10288–10300
48. Damodaran K, Sanjayan GJ, Rajamohanan PR, Ganapathy S, Ganesh KN (2001) Solid state NMR of a molecular self-assembly: multinuclear approach to the cyanuric acid-melamine system. Org Lett 3:1921–1924
49. Huang Z, Li F, Chen B, Yuan G (2014) Nanosheets of graphitic carbon nitride as metal-free environmental photocatalysts. Catal Sci Technol 4:4258–4264
50. Gu L, Wang J, Zou Z, Han X (2014) Graphitic-C3N4-hybridized TiO2 nanosheets with reactive 001 facets to enhance the UV- and visible-light photocatalytic activity. J Hazard Mater 268:216–223